Master Thesis

Signal and background studies for scalar leptoquark pair production in the $t\bar{t} + 2\tau$ channel at the ATLAS experiment

Daniel Adlkofer

Supervisor
Prof. Dr. Raimund Ströhmer

Advisor
Dr. Mahsana Haleem

December 2018

Lehrstuhl für Physik und ihre Didaktik
Physikalisches Institut
Julius-Maximilians-Universität Würzburg

Contents

Summary

Zusammenfassung

1.

XyZ

sample	$t\bar{t}$	$t\bar{t}H$	$LQ_{500\,GeV}$	$LQ_{1\,TeV}$
selection	reconstruction	reconstruction	reconstruction	reconstruction
	event yield	event yield	event yield	event yield
≥ 2 b-jets	186 395	209	152	1.5
≥ 2 b-jets $+ \geq 1\,\tau$	505	7	94	0.9
≥ 2 b-jets $+ \geq 2\,\tau$	1.7	0.4	27	0.2

Table 1.1.: Event yield for different selections with tau leptons for the $t\bar{t}$, the $t\bar{t}H$ and the LQ Monte Carlo sample. The luminosity accounts for $150\,fb^{-1}$.

sample	$t\bar{t}$	$t\bar{t}H$
selection	efficiency $\frac{\epsilon}{\%}$	efficiency $\frac{\epsilon}{\%}$
≥ 2 b-jets	26.52	36.72
≥ 2 b-jets $+1\,\tau$	3.18	8.83
≥ 2 b-jets $+2\,\tau$	1.41	2.13

Table 1.2.: Efficiencies for different selections with tau leptons for the $t\bar{t}$ and the $t\bar{t}H$ Monte Carlo sample.

sample	$t\bar{t}$		$t\bar{t}H$	
selection	reference selection	reconstruction ratio $\frac{r}{\%}$	truth ratio $\frac{r}{\%}$	reconstruction ratio $\frac{r}{\%}$	truth ratio $\frac{r}{\%}$
≥ 2 b-jets $+1\,\tau$	≥ 2 b-jets	0.28	2.35	3.43	14.26
≥ 2 b-jets $+2\,\tau$	≥ 2 b-jets	0.0011	0.020	0.24	4.11

Table 1.3.: Ratios for different selections with tau leptons for the $t\bar{t}$ and the $t\bar{t}H$ Monte Carlo sample.

sample	$t\bar{t}$		$t\bar{t}H$	
selection	numerator event yield	denominator event yield	numerator event yield	denominator event yield
truth matching for tau	63	13723	5590	21610
efficiency	0.46%		25.9%	
tau from H^0, $W^\pm$, Z^0	0	0	4859	11988
efficiency	-		40.5%	
tau from B-mesons	63	13722	20	7416
efficiency	0.46%		0.27%	
tau within a jet	8440	3776952	18511	20327225
efficiency	0.22%		0.091%	
tau within a b-jet	6098	2658379	2317	1208924
efficiency	0.23%		0.19%	

Table 1.4.: Event yield for different selections with tau leptons for the $t\bar{t}$ and the $t\bar{t}H$ Monte Carlo sample. The luminosity accounts for $36.1\,\mathrm{fb}^{-1}$.

sample	LQ$_{500\,\text{GeV}}$		LQ$_{1\,\text{TeV}}$	
selection	numerator event yield	denominator event yield	numerator event yield	denominator event yield
truth matching for tau	2604	5362	2263	5055
efficiency		48.6%		44.8%
tau from H^0, W$^\pm$, Z^0	95	340	82	461
efficiency		27.9%		17.8%
tau from B-mesons	0	183	0	200
efficiency		0.0%		0.0%
tau from LQ	1744	3286	1057	2022
efficiency		53.1%		52.3%
tau within a jet	7232	55208	7011	63671
efficiency		13.1%		11.0%
tau within a b-jet	2317	1208924	6098	2658379
efficiency		0.45%		0.23%

Table 1.5.

2.

Introduction

3.

Theoretical background for the search for scalar leptoquarks

This chapter describes theoretical foundations required for the search for scalar leptoquarks including the successful Standard Model of elementary particle physics evolved from the symbiosis of experimental achievements and theoretical milestones. Besides its success some issues still remain unsolved and could be a hint to physics beyond the Standard Model, giving space to introduce the Leptoquark Model as one possible extension.

3.1. The Standard Model of particle physics

A remarkable development for understanding nature is the Standard Model (SM) of particle physics, embracing physics at the most fundamental level. This quantum field theory, incorporating the conceptual frameworks of special relativity and quantum mechanics, describes the constituents of matter and the laws governing their interactions. [1] Despite its success of being the most promising theory so far capable of explaining the observed results within its domain in agreement with empirical data, it seems not to be the complete story. [2]

One of the most important concept in physics is that of symmetries, because they are deeply connected with conservation laws, following Noether's Theorem. A physical property responds to a symmetry transformation in two different ways. It can appear in form of an invariant under symmetry transformation, leaving that property unchanged, or as covariant, changing their property induced by the symmetry transformation. Fundamental symmetries of particle physics include space

group	defining property	application
$U(n)$	$n \times n$ unitary $(U^\dagger U = 1)$	$U(1)$ electromagnetism
$SU(n)$	$n \times n$ unitary $(U^\dagger U = 1)$ with $\det U = 1$	$SU(2)$ weak interactions $SU(3)$ strong interactions
$SO(n)$	$n \times n$ orthogonal $(O^\intercal O = 1)$ with $\det O = 1$	$SO(3)$ rotations $SO(3,1)$ Lorentz transformations

Table 3.1.: Lie symmetry groups for the gauge interactions of the Standard Model [1].

translation symmetry and hence the conservation of momentum, rotational invariance and hence conservation of angular momentum and time translation invariance leading to energy conservation. The formal mathematical description for fundamental symmetries is based on group theory. In case of particle physics almost all groups are Lie groups $\mathcal{G}$, that are a set of objects $\{g_i\}$, which can be combined with a binary operation and has four basic properties: closure, identity, inverse element and associativity. Additionally, the group elements are continuous and differentiable functions of some finite set of parameters θ_a:

$$g = g(\theta_1, \ldots, \theta_N) = \exp\left[i\theta_a \mathbf{T}^a\right] = \exp\left[i\vec{\theta}\vec{\mathbf{T}}\right] \qquad \text{with} \quad a = 1, \ldots, N \qquad (3.1)$$

Here $\mathbf{T}^a$ are the generators of the group from which all elements of the group can be created. The irreducible representatives of a group can be written as complex matrices*, acting on the wave function of the particles and on charges as well as on space-time coordinates. [1] The local symmetry $SU(3)_c \times SU(2)_L \times U(1)_Y$ summarizes the gauge interactions of the SM (see table 3.1). Here c indicates the strong force, L the left handed chirality of the weak regime and $Y = B + s$ the hypercharge calculated from baryon number B and strangeness s. [3] Besides the continuous symmetries above also important discrete symmetries exist in the SM like parity P, referring to the transformation $\vec{x} \rightarrow -\vec{x}$, time reversal T, referring to $t \rightarrow -t$, and charge conjugation C, corresponding to the exchange of a particle

---

*Irreducible means that not all representing matrices of the group can be decomposed into block-diagonal form simultaneously [1].

with its anti-particle. The weak force breaks P and C, but not the product of CPT. [2]

Matter and its interactions can be described by two basic types of particles and four fundamental forces, i.e. the electromagnetic force, the weak and the strong force and gravity. Fermionic particles, following Fermi-Dirac statistics, make up matter, whereas bosons, following Bose-Einstein statistics, are acting as mediators of the fundamental forces. [4][5]
The fermions can be further categorized into 6 leptons l characterized through the lepton quantum number L_l and 6 quarks q characterized through the baryon quantum number B together with their anti-particles ($\bar{l}$ respectively $\bar{q}$). The difference between particle and anti-particle are the contrary charges and contrary lepton and baryon number respectively, whereas mass, mean lifetime and spin stay the same. Leptons occur in three generations with different flavor – electron (e), muon (μ) and tauon (τ) – and can carry electrical charge $Q = \pm e$ in units of the elementary charge. The electrically neutral leptons are the neutrinos ν_l. [5]
Table 3.2 shows the leptons with selected properties.
The quarks also occur in three generations and carry electrical charge of either $Q = \mp\frac{1}{3}e$ or $Q = \pm\frac{2}{3}e$ in units of the elementary charge as well as color charge. The new type of charge can be introduced, because the quarks lie in the fundamental representation of $SU(3)$. Possible color charges are red, green and blue and the additional anti-colors indicate that quarks are interacting with the strong force among the electromagnetic and weak interaction. [5] Quarks only occur confined in color-neutral compound systems called hadrons. Baryons are three-quark hadronic states with baryon number 1 and mesons are quark-anti-quark hadronic states, having a baryon number of 0. [4] The reason for quark confinement can be found in the potential $V(r)$ between quarks and anti-quarks depending on distance r. The potential has the shape $V(r) \propto \frac{-1}{r} + \text{const} \cdot r$. When separating a quark-anti-quark pair, additional potential energy must be supplied, which can exceed the potential $V(R) > 2m_q$ for more than two quark masses at distance R. Quantum fluctuations result in the origin of a new quark pair in between. The final state now consists of two pairs, again externally color-neutral. [2] Table 3.2 shows the different quark flavors up, down, charm, strange, top and bottom with some characteristic properties. The bosons shown in table 3.2 are the quanta of the fundamental forces [4]:

- The photon γ is the mediator of the electromagnetic force.

- Three mediators Z^0, W^+ and W^- for the weak force.

leptons

l	L_l	B	Q/e	$m/\frac{\text{GeV}}{c^2}$	Spin $S_z/\hbar$
e^-	$L_e = 1$	0	-1	0.511	$\frac{1}{2}$
ν_e	$L_e = 1$	0	0	$< 2 \cdot 10^{-6}$	$\frac{1}{2}$
μ^-	$L_\mu = 1$	0	-1	106	$\frac{1}{2}$
ν_μ	$L_\mu = 1$	0	0	$< 2 \cdot 10^{-6}$	$\frac{1}{2}$
τ^-	$L_\tau = 1$	0	-1	$1.78 \cdot 10^3$	$\frac{1}{2}$
ν_τ	$L_\tau = 1$	0	0	$< 2 \cdot 10^{-6}$	$\frac{1}{2}$

quarks

q	L_l	B	Q/e	$m/\frac{\text{GeV}}{c^2}$	Spin $S_z/\hbar$
u (up)	0	$\frac{1}{3}$	$\frac{2}{3}$	2.2	$\frac{1}{2}$
d (down)	0	$\frac{1}{3}$	$-\frac{1}{3}$	4.7	$\frac{1}{2}$
c (charm)	0	$\frac{1}{3}$	$\frac{2}{3}$	$1.3 \cdot 10^3$	$\frac{1}{2}$
s (strange)	0	$\frac{1}{3}$	$-\frac{1}{3}$	95	$\frac{1}{2}$
t (top)	0	$\frac{1}{3}$	$\frac{2}{3}$	$17 \cdot 10^4$	$\frac{1}{2}$
b (bottom)	0	$\frac{1}{3}$	$-\frac{1}{3}$	$4.2 \cdot 10^3$	$\frac{1}{2}$

gauge bosons

boson	L_l	B	Q/e	$m/\frac{\text{GeV}}{c^2}$	Spin $S_z/\hbar$
γ	0	0	0	0	1
Z^0	0	0	0	91.2	1
W^-	0	0	-1	80.4	1
W^+	0	0	$+1$	80.4	1
g	0	0	0	0	1
H^0	0	0	0	125	0

Table 3.2.: Overview of leptons l, quarks q and gauge bosons as mediators of the fundamental forces with some selected properties and quantum numbers like electrical charge Q, mass m, lepton number L_l and baryon number B. [2][6]. The fermion anti-particles are not shown, which would have opposite charges and lepton/baryon number.

- 8 colored gluons as mediators for the strong force.

- The Higgs boson H^0 as quantum of the Higgs field, providing the masses for the elementary particles.

At the current state of research a quantum field theory of gravity is purely hypothetical. The mediator for such theory would be the graviton (see chapter 3.2). A second aspect is that on elementary particle scales gravity is insignificant compared[†] to all other forces and is therefore not originally considered in the SM. [4]
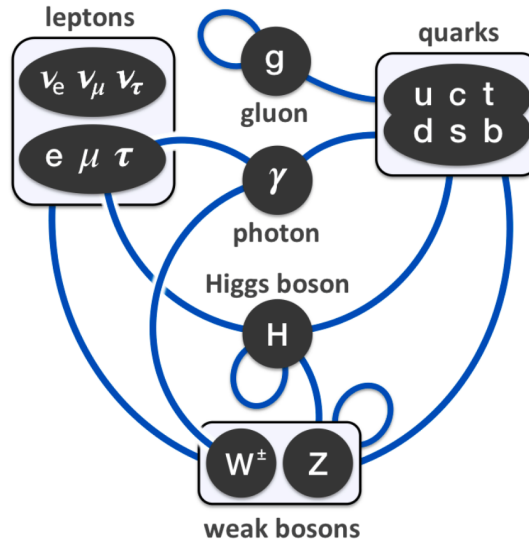
Figure 3.1.: The Standard Model with its fermions and bosons and the involved interactions. The solid blue line indicates which particles interact with each other. Loops depict self-interaction. [7]

Figure 3.1 summarizes the picture of the SM with its fermions and bosons. The lines indicate which particles interact with each other through the mediators, including self-interaction.

[†]Relative strength of gravity compared to the weak interaction is 10^{-35} [1].

3.2. Beyond the scope of the Standard Model

Nevertheless, there are still many puzzles left which are not described by the SM. This circumstance keeps physicists well motivated to gain further progress and to push the frontiers of our understanding. [2] In the following some of the issues are briefly described, like neutrino masses, quantum gravity, the hierarchy problem and supersymmetry.

Neutrino masses are confirmed by various neutrino oscillation experiments [8][9], although the SM does not predict neutrino masses. The neutrino flavor states ν_α with $\alpha = e, \mu, \tau$ are quantum entangled with the mass states ν_i where $i = 1, 2, 3$ described by an unitary matrix $U_{\alpha i}$ [10]. One possible extension of the SM, explaining neutrino masses, is the seesaw mechanism. Because of the absence of the right chirality spinor components $\Psi_{R,j}$, the mass term of the Dirac lagrangian $\bar\Psi_L \Psi_R + \bar\Psi_R \Psi_L$ cannot be formed in case of neutrinos. One possible solution is to describe the neutrino masses with a Majorana mass term, which introduces very massive right-chiral neutrinos* besides light weight left-chiral neutrinos. One caveat is that such right-chiral neutrinos as a consequence have to exist, although within the SM there are only left-handed neutrinos known. [2]

Quantum gravity could be the embedding of general relativity into a framework of quantum theory. Quantum theory provides a well confirmed framework for all theories describing particular interactions. Therefore it would be appealing to have a quantum formulation of gravity, following the example of all other fundamental forces and being one step closer to an unified description. From the point of view of cosmology, quantum gravity could be an encompassing theory for a more fundamental understanding where general relativity breaks down, when it comes to the initial conditions of the early universe or conditions of black holes. [11]

The hierarchy problem is a current challenge in particle physics and arises from quadratic corrections to the weak scale. [12] The hierarchy problem formulates the

---

*The large masses are consistent with the lack of evidence for right-chiral neutrinos at present day energies [2].

large differences of scales at which symmetries are broken. Considering a single, unifying symmetry, including the standard model symmetries $SU(3)_c \times SU(2)_L \times U(1)_Y$ (see chapter 3.1), which has to be broken at scale V, because it is not manifested at the currently explored energy scales. A lower bound is $V \approx 10^{37}\,\text{GeV}$. At the same time spontaneous symmetry breaking takes place for $SU(2)_L \times U(1)_Y$ at scales of $v \approx 246\,\text{GeV}^\dagger$ in order to allow for massive $\text{W}^\pm$ and Z^0 bosons as well es massive quarks and leptons. Within the framework of perturbation theory in quantum field theory such great scale differences are difficult to keep due to the fact that corrections of symmetry breaking are controlled by the highest masses involved. One approach for v is $v^2 = v_0^2 \sum_{i=1}^{k} c_i \lambda^i V_0^2$ with the initial value v_0, the coupling constant λ and general coefficients c_i. This shows that including the first order of correction, the equation becomes $v^2 = v_0^2 + c_1 \lambda V_0^2$. The consequence is that v_0^2 has to be adjusted in such a way that it cancels out several decimal places, for instance 25, of the term $c_1 \lambda V_0^2$, but the decimal places beyond that limit should add up to the scale of $246\,\text{GeV}$. This fine tuning is an unsatisfactory situation, even worsened by adding more orders of quantum corrections. [2] A non-perturbative solution to the hierarchy problem is proposed by supersymmetric models. [14]

Supersymmmetry (SUSY) is a theory, which unifies fermions and bosons. The corresponding transformation can be described by an operator in spinor form $Q_{\alpha i}$ and converts fermion fields into boson fields and vice versa. Here α is the spinor index and i are internal degrees of freedom. The field pairs are called superpartners (sparticles) and belong to the same multiplet. The difference between particles and sparticles is the spin quantum number which distinguishes them by half an unit of $\hbar$. [15] Due to the lack of evidence of sparticles in the same mass range as the already known elementary particles, also supersymmetry has to be broken. [3]. SUSY is very attractive, because it can solve the hierarchy problem, achieve gauge unification and can even provide a candidate for dark matter. [16] There are two main categories of supersymmetric models, namely R-parity conserving and R-parity violating models. R is a discrete symmetry in the coupling of particles and their superpartners, defined as [15]:

$$R = (-1)^{2S+3B+L} = \begin{cases} +1 & \text{for ordinary particles} \\ -1 & \text{for SUSY particles} \end{cases}, \tag{3.2}$$

---

†This is the vacuum expectation value for the Higgs field. [13]

where S is the spin, B the baryon number and L the lepton number. An exactly conserved R-parity will result in a stable lightest supersymmetric particle and the SUSY particles will be produced in pairs. Whereas a R-parity violation will result in singly producable sparticles and all of them are intrinsically unstable. [17]

3.3. Leptoquarks

Different shortcomings of the Standardmodel open up chances to extend the current understanding of elementary particle physics with concepts briefly introduced in chapter 3.2. One basic idea develops the symmetry approach further, taking the current symmetries as an example (see chapter 3.1), into a grand unified theory (GUT). This can be made possible by embedding the SM gauge groups $SU(3)_c \times SU(2)_L \times U(1)_Y$ into a higher symmetry G_{GUT}. This group has to be broken at the so called GUT-scale of $\sim 10^{16}$ GeV to such an extent that the three SM interactions occur as separate interactions below this scale. [3] The previously mentioned issues in chapter 3.2 already gave a clue on this unification concept in different degrees of manifestations and show that GUT can be a solution for different issues, for example the gauge hierarchy problem [18][19], the generation problem [19], the parameter problem [19] and neutrino masses [20]. GUTs imply new gauge bosons called leptoquarks (LQ), which would explain the strong similarities between leptons and quarks. [16]

3.3.1. Leptoquarks and grand unified theories

The first GUT model was proposed by Georgi and Glashow in 1974 [21]. They proposed that the group $SU(5)$ incorporates all the fermions into one multiplet following the same universal coupling. This enables the possibility to transform leptons and quarks into each other with leptoquarks as mediators. Various global symmetries can embed the SM symmetries, but $SU(5)$ is the simplest one. [22] Altough the Georgi-Glashow model had a great impact, this model has been ruled out [23]. It

predicts a lifetime of the proton of 10^{30} years, but the current experimental lower limit is 10^{33} years[*] [5][24].

Another unifying group would be $SO(10)$, which is broken to $SO(10) \rightarrow SU(4)_c \times SU(2)_L \times SU(2)_R$, where the leptons are treated as a forth color. [25] This model is knwon as Pati-Salam GUT model [26]. Here also the right-handed leptons are included, acting differently than their left-chiral counterparts as it is expected for solutions of the neutrino masses for example. [25]

Other symmetry groups like E_6, inspired by superstring models, are also candidates for a GUT theory. [27] E_6 has a rank of 6 and is a member of the exceptional Lie groups. Furthermore it can be seen as the natural extension of $SU(5)$ and $SU(10)$ and naturally includes a greater set of particles. These additional particles can be, for instance, interpreted as dark matter candidates. [28]

3.3.2. Effective Leptoquark model

All the GUT models, which are briefly mentioned in section 3.3.1, share a common implication, namely the introduction of new gauge bosons called leptoquarks. This implication can be formulated as an effective theory of leptoquarks for energy scales below the GUT-scale , describing the underlying physical concepts.

The introduction of the effective leptoquark model closely follows [17].
Leptoquarks are color-triplet scalar (S) or vector (V) bosons having baryon and lepton numbers and carrying fractional electrical charge. [17] A general formulation of an effective Lagrangian for leptoquark interaction with SM fermions was proposed by Buchmüller, Rückl and Wyler [29]. It assumes the follwing:

(i) LQs have renormalizable interactions.

(ii) LQs have interactions invariant under the SM gauge symmetries $SU(3)_c \times SU(2)_L \times U(1)_Y$.

---

[*]This value is vaild for the decay mode $p \rightarrow e^+ K^0$. The predictions of the proton lifetime for other dominant decay modes – relevant in GUT models – are higher and can be found in reference [24].

$|F| = 2$ leptoquarks				$|F| = 0$ leptoquarks			
LQ	Q/e	T_3	decay	LQ	Q/e	T_3	decay
$S_{0,L}$	$-1/3$	0	$l_L^- u_L$ or $\nu_L d_L$	$V_{0,L}$	$-2/3$	0	$l_L^- \bar{d}_R$ or $\nu_L \bar{u}_R$
$S_{0,R}$			$l_R^- u_R$	$V_{0,R}$			$l_R^- \bar{d}_L$
$\tilde{S}_{0,R}$	$-4/3$	0	$l_R^- d_R$	$\tilde{V}_{0,L}$	$-5/3$	0	$l_R^- \bar{u}_L$
$S_{1,L}$	$-4/3$	-1	$l_L^- d_L$	$V_{1,L}$	$-5/3$	-1	$l_L^- \bar{u}_R$
	$-1/3$	0	$l_L^- u_L$ or $\nu_L d_L$		$-2/3$	0	$l_L^- \bar{d}_R$ or $\nu_L \bar{u}_R$
	$2/3$	1	$\nu_L u_L$		$1/3$	1	$\nu_L \bar{d}_R$
$V_{1/2,L}$	$-4/3$	$-1/2$	$l_L^- d_R$	$S_{1/2,L}$	$-5/3$	$-1/2$	$l_L^- \bar{u}_L$
$V_{1/2,R}$	$-4/3$		$l_R^- d_L$	$S_{1/2,R}$	$-5/3$		$l_R^- \bar{u}_R$
	$-1/3$	$1/2$	$l_R^- u_L$		$-2/3$	$1/2$	$l_R^- \bar{d}_R$
$\tilde{V}_{1/2,L}$	$-1/3$	$-1/2$	$l_L^- u_R$	$\tilde{S}_{1/2,L}$	$-2/3$	$-1/2$	$l_L^- \bar{d}_L$
	$2/3$	$1/2$	$\nu_L u_R$		$1/3$	$1/2$	$\nu_L \bar{d}_L$

Table 3.3.: Overview of the scalar (S) and vector (V) leptoquarks proposed by the minimal-Buchmüller-Rückl-Wyler model with their third component of the weak isospin T_3, electric charge Q and fermion number F. The fourth column shows possible decay modes of the leptoquarks. [17]

(iii) LQs couple only to the SM fermions, gauge bosons and the Higgs boson.

(iv) LQs are required to conserve the lepton number L and the baryon number B separately. They carry the fermion number

$$F = 3B + L \qquad (3.3)$$

with $|F| = 0$ or $|F| = 2$.

(v) Each LQ couples to only one quark-lepton generation, i.e. there are three LQ families.

(vi) LQs has pure chiral couplings to the SM fermions.

Condition (iv) makes sure that the proton instability is avoided. Condition (v) only allows inter-generational interactions and large tree-level flavor changing neutral currents and flavor universalities. Condition (vi) avoids direct contributions to chirally supressed meson decays like $\pi \to e\nu$. The LQ model, fulfilling conditions (i)-(vi), is the so called minimal-Buchmüller-Rückl-Wyler effective model (mBRW) with the Yukawa coupling[†] constant λ. [17]

Fourteen different leptoquark types are proposed and are listed in table 3.3. The same symbol represents LQs of different electric charge within an isospin family, i.e. $S_{1/2,L}$ stands for both, the $S_{1/2}$ state of charge $-\frac{5}{3}$ and for $-\frac{2}{3}$. Here l_X are the left-handed lepton doublets in case of $X = L$ and the right handed lepton singlet in case of $X = R$. This differentiation between left-chirality and right-chirality is also valid for the quarks q_X of up-type ($q = u$) or down-type ($q = d$). Seven of the fourteen LQs are scalars ($S_{0,L}$, $S_{0,R}$, $\tilde{S}_{0,R}$, $S_{1,L}$, $S_{1/2,L}$, $S_{1/2,R}$, $\tilde{S}_{1/2,L}$) and seven are vectors ($V_{0,L}$, $V_{0,R}$, $\tilde{V}_{0,R}$, $V_{1,L}$, $V_{1/2,L}$, $V_{1/2,R}$, $\tilde{V}_{1/2,L}$) with their fermion number $|F| = 0$ and $|F| = 2$. For specific models based on mBRW the branching ratio $\beta(LQ \to lq)$ is usually fixed to values like 0, $\frac{1}{2}$ or 1. [17]

From the experimentalists' point of view it makes sense to expand the phenomenology of leptoquarks and ease some restrictions of the mBRW model, giving rise to more generic models. This means a broader sensitivity to possibly new physics in the face of already determined exclusion limits. One example is to consider the

---

[†]Yukawa coupling describes the interaction of a scalar field with a scalar or pseudoscalar Dirac field [30].

branching ratio β as a free parameter. Relaxing condition (iv) or (v) in the lepton sector could open new lepton-flavor violating decays. As a result the search for leptoquarks is more sensitive to various possibilities in the decay modes or the restrictions LQ-coupling. [17]

3.3.3. Leptoquark-like couplings in supersymmetry

An additional generic picture can result from the point of view of supersymmetry. In R-parity violating SUSY models squarks can produce leptoquark-like signature due to decay modes involving the Yukawa coupling. The left-chiral $\tilde{u}_L{}^{\ddagger}$ squark couples to a $e^+ + d$ pair similar a leptoquark $\tilde{S}_{1/2,L}$ with an electric charge of $|Q| = \frac{2}{3}e$ would do. Accordingly the $\tilde{d}_R$ squark couples to a $e^- + u$ pair or $\nu_e + d$ pair and mimics a S_0 leptoquark of charge $|Q| = \frac{1}{3}e$. From an experimental point of view, the observation of such a decay is not only restricted to LQ models, but also has implications on constraints for the coupling of squarks in SUSY models. [17]
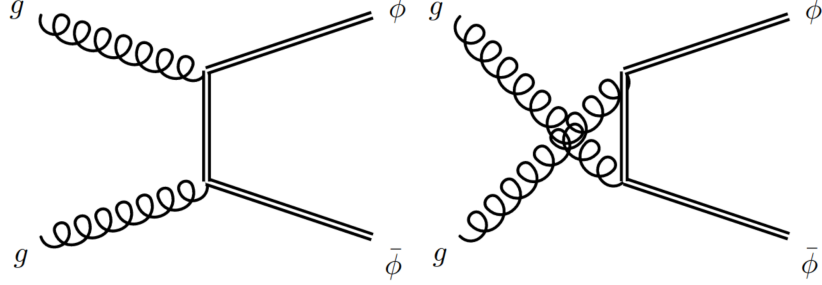
3.3.4. Leptoquark pair production in proton-proton collisions

For the search of leptoquarks, the mBRW model (see chapter 3.3.2) is taken as a basis.

At proton-proton colliders, like the LHC, leptoquarks can be be produced in pairs by gluon-fusion and smaller contributions of quark-fusion. These main processes are shown with feynman diagrams in figure 3.2. Figure 3.2a and 3.2b describes the gluon initiated production in the s-, t- and u-channel and figure 3.2c the quark initiated production in the s- and t-channel. The last feynman diagram (lower right) is proportional to the square of the coupling constant (λ^2) due to the virtual lepton exchange [31][32]. Cross section calculations for such processes and further details can be found for example in reference [33]. The detectable final states are governed by the Yukawa coupling λ_{lq} of the leptoquark directly to the quark q and lepton l (see figure 3.3). The model is defined by two parameters derived from λ_{lq}: The branching ratio β and the coupling constant λ. They are connected to the Yukawa
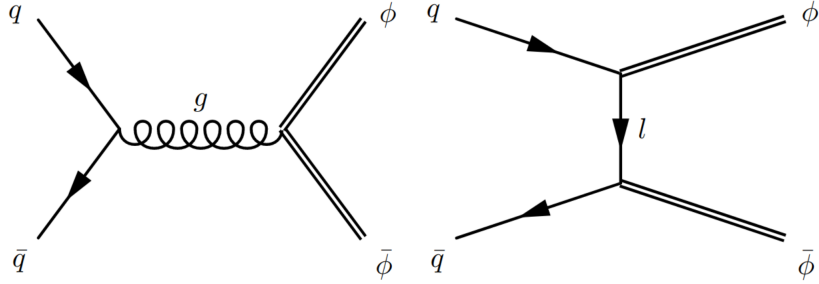
---

‡Usually the supersymmetric partner particles are denoted with a tilde ($\tilde{}$).

(a) Leptoquark pair production via gluon-fusion in the t-channel and the u-channel.
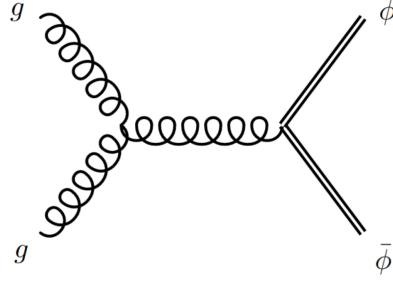

(b) Leptoquark pair production via gluon-fusion in the s-channel.

(c) Leptoquark pair production via quark-fusion in the s-channel and the t-channel.

Figure 3.2.: Feynman diagrams of leptoquark pair production processes dominated by gluon-fusion (a), (b) and smaller contributions by quark-fusion (c) at proton-proton colliders like the LHC. [31]

coupling constant by $\lambda_{lq} = \sqrt{\beta}\lambda$ for a charged lepton and by $\lambda_{lq} = \sqrt{1-\beta}\lambda$ for neutrinos. [34]
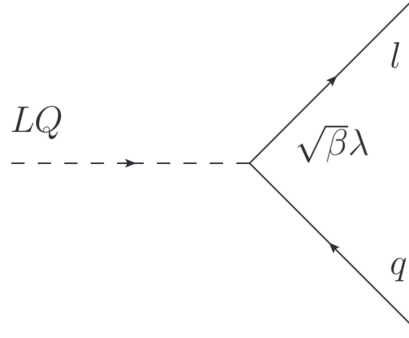
Figure 3.3.: Feynman diagrams of a leptoquark decay into a lepton l and a quark q gouverned by Yukawa coupling $\lambda_{lq} = \sqrt{\beta}\lambda$. [34]

The focus of this thesis lies on the search of pair produced scalar leptoquarks with the final state $LQ + LQ \rightarrow t\tau^- + \bar{t}\tau^+$. These final states would correspond to leptoquarks $S_{0,L}$ and $S_{1,L}$ (cf. table 3.3).

3.3.5. Current status in the search for scalar leptoquarks

Leptoquarks are a promising research field for physics beyond the SM. Various efforts are made with today's particle accelerators to search for LQ-like signatures. The following summarizes briefly the current status for the search of scalar leptoquarks at the LHC.

LQ considered by the minimal-Buchmüller-Rückl-Wyler model (cf. section 3.3.2) can result in various final states, which can be potentially detected by the ATLAS or CMS detector.
Simulated signal events of pair-produced LQs decaying to $LQ + LQ \rightarrow e^+q + e^-\bar{q}$, $LQ + LQ \rightarrow \mu^+q + \mu^-\bar{q}$, $LQ + LQ \rightarrow t\nu_\tau + q + \bar{t}\bar{\nu}_\tau$ and $LQ + LQ \rightarrow b\nu_\tau + q + \bar{b}\bar{\nu}_\tau$ were compared with $\sqrt{s} = 8$ TeV data samples of the ATLAS detector at an integrated luminosity of 20.3 fb^{-1} for first and second generation LQs ($e^+qe^-\bar{q}$ and $\mu^+q\mu^-\bar{q}$ channel). The integrated luminosity for the search of third generation LQs ($t\nu_\tau\bar{t}\bar{\nu}_\tau$

and $b\nu_\tau \bar{b}\bar{\nu}_\tau$) is $20.1\,\text{fb}^{-1}$. [35] For a branching ratio of the LQs of $\beta = 1.0$ exclusion limits have been found for the first and second generation LQs. The exclusion limit for first generation LQ masses are $m_{LQ1} < 1050\,\text{GeV}$ and for second generation LQ masses are $m_{LQ2} < 1000\,\text{GeV}$ at a confidence limit (CL) of 95 %. For third generation the mass exclusion limit at CL 95 % is $m_{LQ3} < 625\,\text{GeV}$ based on the $b\nu_\tau \bar{b}\bar{\nu}_\tau$ decay mode and $210\,\text{GeV} < m_{LQ3} < 640\,\text{GeV}$ based on the $t\nu_\tau \bar{t}\bar{\nu}_\tau$ decay mode. [35]

A more recent study of the ATLAS collaboration at $\sqrt{s} = 13\,\text{TeV}$ was published in reference [34] for first and second generation leptoquarks. The observerd exclusion limits for the LQ mass at 95 % CL are $1100\,\text{GeV}$ and $1050\,\text{GeV}$ assuming a branching ratio of $\beta = 1.0$. The study has increased sensitivity for the leptoquarks and agrees with the former study [35]. At least, the exclusion limits are extended [34] compared to the previous study.

The CMS collaboration published a study for the search of third generation scalar leptoquarks decaying to a top quark and τ-lepton at a center of mass energy of $13\,\text{TeV}$. The corresponding integrated luminosity is $35.9\,\text{fb}^{-1}$. The results agree
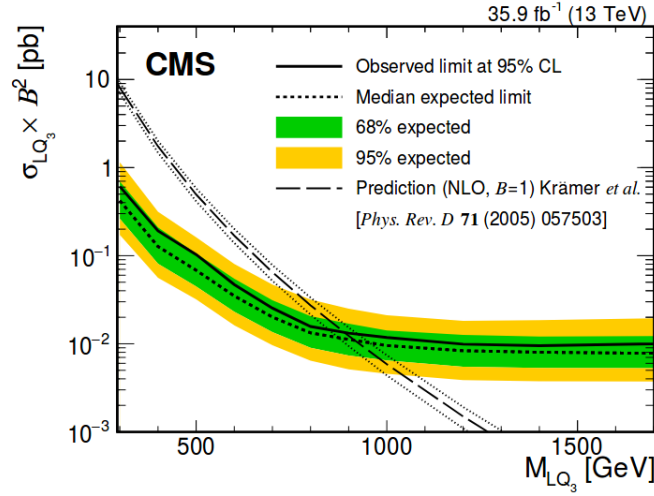
Figure 3.4.: Upper limits at CL 95 % of the product of the cross section and β^2 depending on the leptoquark mass for the $t\tau^- \bar{t}\tau^+$ channel (third generation) at $\sqrt{s} = 13\,\text{TeV}$ [34].

with the standard model expectation and no evidence for LQ pair production was
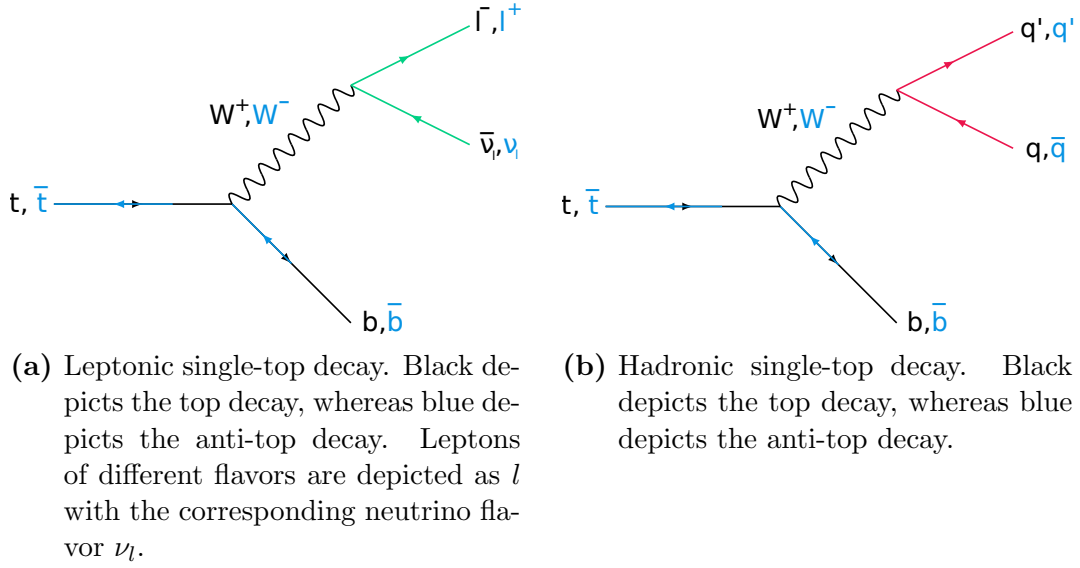
found. The study excludes LQ with masses below $900\,\text{GeV}$ at a branching fraction of $\beta = 1.0$ and at a CL of $95\,\%$. Figure 3.4 shows upper limits at CL $95\,\%$ of the product of the cross section and β^2 depending on the leptoquark mass for the $t\tau^- \bar{t}\tau^+$ channel. These results are the most stringent limits to date for the production of third generation LQs decaying to top quark and τ-lepton. [36]

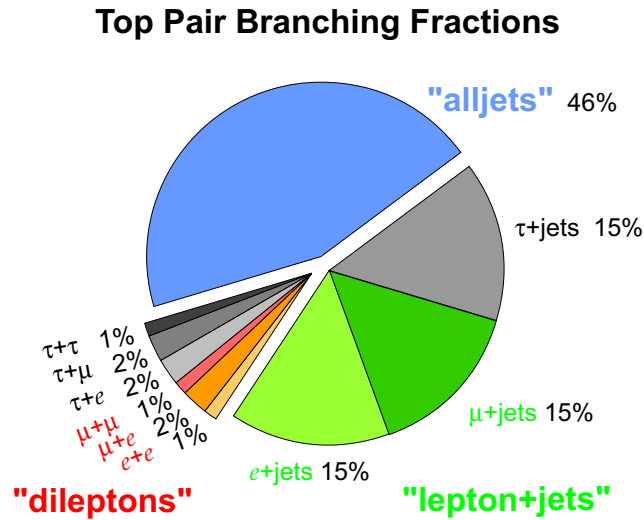## 3.3.6. Starting point and research question for the analysis

This work has to be seen in the general research context briefly described in section 3.3.5 and makes a contribution to the search of pair-produced scalar LQs of type $S_{0,L}$ and $S_{1,L}$ (cf. table 3.3) decaying to $LQ + LQ \rightarrow t\tau^- + \bar{t}\tau^+$ at the ATLAS experiment. This involves in particluar τ reconstruction efficiencies and background studies for the search of LQ-signal signatures based on MC samples. The simulations are compared with data from the data taking periods 2015, 2016, 2017 and partly 2018 adding up to an integrated luminosity of $128.34\,\text{fb}^{-1}$.

The search for third generation LQ decaying to top quarks and τ-leptons is complex because of the multiple objects resulting from the final states of the heaviest quark and heaviest lepton. The top quark decays weakly into $t \rightarrow Wq$ with $q = b, s, d$. The main decay mode involves the bottom quark. The subsequent decay of the weak gauge boson W is either hadronically $((66.5 \pm 1.4)\,\%)$ or leptonically $((34.0 \pm 1.0)\,\%)$ [6]. This is shown in figure 3.5, where the black diagram paths is for the top decay and the blue diagram path for the anti-top decay. Leptons of different flavors are depicted as l with their corresponding neutrinos ν_l. This means that top-pairs can produce full-leptonic decays following both the feynman diagram of figure 3.5a, full-hadronic decays following both the feynman diagram of figure 3.5b and semi-leptonic decays, where one top decays leptonically and one hadronically. The overall percentage of the final state of evolving from top pair is shown in figure 3.6.

Tau leptons have various decay modes, which can be categorized with the number of charged particles involved in the decay. Main decay modes for taus include one charged particle ('1-prong') and three charged particles ('3-prong') in the decay. They are shown in table 3.4 for τ^-. Here $h^{\pm}$ are charged pions $\pi^{\pm}$ and Kaons $K^{\pm}$, 'neutrals' are photons γ or neutral pions π^0. The decay modes of the τ^+ involve the same products, but with opposite charges.

(a) Leptonic single-top decay. Black depicts the top decay, whereas blue depicts the anti-top decay. Leptons of different flavors are depicted as l with the corresponding neutrino flavor ν_l.

(b) Hadronic single-top decay. Black depicts the top decay, whereas blue depicts the anti-top decay.

Figure 3.5.: Leptonic (a) and hadronic (b) single-top decay.

Figure 3.6.: Branching fractions of top-pairs decaying full-hadronically ('alljets'), full-leptonically ('dileptons') and semi-leptonically ('lepton+jets') [37].

Signal and background studies with various objects in the final state depend crucially on the purity of the signatures left in the detector (cf. chapter 5) and how they are traced back to the potential LQ. Electrons and muons provide a good chance for reliable reconstruction (see chapter 5). Therefore the dilepton and semileptonic decay modes of the top quark-pair are good candidates to study the signal and background contributions for the search of LQ. They provide, additionally to the hadronic τ final states, two leptons from the top-pair decay or one lepton and one jet respectively. In the face of high contributions from underlying QCD events, resulting in jet objects, dilepton and semileptonic modes are easier to reconstruct compared to the full hadronic decays with jets only in the final state. This provides the starting point for studying the hadronic τ reconstruction efficiencies and the influence of fake rates on the $t\tau^- + \bar{t}\tau^+$ channel.

	mode	fraction Γ_i/Γ
	1-prong decay	
Γ_1	particle$^- \geq 0$ neutrals $\geq 0 K_L^0 \nu_\tau$	$(84.58 \pm 0.06)\,\%$
Γ_2	$\mu^- \bar{\nu}_\mu \nu_\tau$	$(17.39 \pm 0.04)\,\%$
Γ_3	$e^- \bar{\nu}_e \nu_\tau$	$(17.82 \pm 0.04)\,\%$
Γ_4	$h^- \nu_\tau$	$(11.51 \pm 0.05)\,\%$
Γ_5	$h^- \geq 1\pi^0 \nu_\tau$ (exluding K^0)	$(36.51 \pm 0.09)\,\%$
Γ_6	$h^- \pi^0 \nu_\tau$	$(25.93 \pm 0.09)\,\%$
Γ_7	$h^- \geq 2\pi^0 \nu_\tau$	$(10.81 \pm 0.09)\,\%$
Γ_8	$h^- 2\pi^0 \nu_\tau$	$(9.48 \pm 0.10)\,\%$
	3-prong decay	
Γ_9	$h^- h^- h^+ \geq 0$ neutrals $\geq 0 K_L^0 \nu_\tau$	$(15.21 \pm 0.06)\,\%$
Γ_{10}	$h^- h^- h^+ \geq 0$ neutrals ν_τ (ex. $K_S^0 \to \pi^+\pi^-$)	$(14.55 \pm 0.06)\,\%$
Γ_{11}	$h^- h^- h^+ \nu_\tau$	$(9.80 \pm 0.05)\,\%$
Γ_{12}	$\pi^- \pi^+ \pi^- \nu_\tau$	$(9.31 \pm 0.05)\,\%$
Γ_{13}	$h^- h^- h^+ \geq 1\pi^0 \nu_\tau$ (excluding K^0)	$(5.09 \pm 0.05)\,\%$
Γ_{14}	$h^- h^- h^+ \pi^0 \nu_\tau$	$(4.76 \pm 0.05)\,\%$
Γ_{15}	$\pi^- \pi^+ \pi^- \pi^0 \nu_\tau$	$(4.57 \pm 0.05)\,\%$

Table 3.4.: Main decay modes of τ^- including one charged particle ('1-prong') and three charged particles ('3-prong'). $h^\pm$ are charged pions $\pi^\pm$ and Kaons $K^\pm$, 'neutrals' are photons γ or neutral pions π^0. The decay products of τ^+ have opposite charges correspondingly. [6]

4.

Experimental setup for the search for scalar leptoquarks

For the search for scalar leptoquarks the ATLAS detector at the Large Hadron Collider (LHC) is used as experimental setup, which will be described within this chapter. The general setting of the proton-proton collider located at the CERN research center is the topic of section 4.1. The particle detection of the resulting collision events, taking place in the ATLAS detector with its different specialized components (section 4.2). Section 3.3.4 addresses the possible leptoquark pair production in proton-proton collisions.

4.1. The Large Hadron Collider accelerator complex

The CERN (Conseil Européen pour la Recherche Nucléaire) research center was founded in 1954 and is located near Geneva, Switzerland. It became a major European joint venture on elementary and nuclear particle physics. Currently, 22 member states are participating in that large-scale project. The scientific ambition is manifold and includes to probe the essential constituents of nature and the fundamental forces acting between them. [38]

In the accelerator complex protons reach energies of $6.5\,\mathrm{TeV}$ by going through different accelerator stages and are brought to collisions at defined interaction points in time intervals of $25\,\mathrm{ns}$. Particle detectors, which are positioned at these interaction points, then register signatures of the resulting collision events and the analysis of newly created particles gives insight to the nature of elementary particle physics.[40] The LHC is designed as two-ring proton-proton collider. It is also possible to collide

Figure 4.1.: Schematic of the CERN accelerator complex with its different stages and few experiments like ATLAS located at the interaction points of the LHC. [39]

lead ions. These ion collisions are provided for the ALICE[41] experiment. However, the ATLAS and CMS experiment are in principle also capable of measuring lead collisions, but currently they are focused mainly on proton events. Figure 4.1 shows the different acceleration stages of the LHC among other CERN experiments.
A hydrogen bottle is the starting point of the proton injection and acceleration. Fully ionized by an electron gun in chambers the protons are guided with electric fields towards the first acceleration stages. Radiofrequency (RF) cavities are responsible for the proton acceleration. Moreover the protons are accelerated in packages, known as bunches. [40][42] Starting from the injection, protons will gain a kinetic energy of 50 MeV in the linear accelerator LINAC2 and will be further transferred to the Proton Synchrotron Booster (1.4 GeV), the Proton Synchrotron (25 GeV), the Super Proton Synchrotron (450 GeV) and finally to the LHC ring with its 26.7 km circumference. [38] Dipole magnets are responsible for directing the protons through the stages and keep them on closed paths. Quadrupole magnets focus the beam to compensate the repulsive forces between the particles and to ensure small beam diameters at the interaction points for high collision rates. Conditions for a stable proton beam are diverse, including high vacua of 10^{-10} mbar to 10^{-11} mbar to avoid collisions with gas atoms and temperatures of 1.9 K for the superconducting NbTi-magnets of the accelerator. [40][42]

Different experiments like ALICE[41], LHCb[43] are located at the LHC due to the variety of research questions. The general-purpose detectors ATLAS and its counterpart CMS[44] are specialized to high luminosities*, exploiting the large range of physics opportunities made possible by the LHC. Main tasks of the ATLAS experiment are precision measurements of the SM (see chapter 3.1), a better understanding of Quantum Chromo Dynamics (QCD) and the search for supersymmetric models, and new physics, among others. With the LHC collision rate of 10^9 inelastic events per second, up to 23 simultaneous events per bunch-crossing at dominating high QCD cross sections reqire a powerful detector that is capable of recognizing the characteristic signatures. These circumstances are the reasons for the demands on the ATLAS detector, including fast electronic elements, high detector granularity, handling high particles fluxes and reducing overlapping events at a large acceptance and coverage region. [45]

---

*For the physical definition see eq. (4.2).

4.2. The ATLAS detector at the LHC

One of the general purpose detectors for proton-proton collisions is the ATLAS detector. This 25 m tall detector is located at one interaction point of the LHC where bunches, consisting of approximately 10^{11} protons, collide at a rate of 40 MHz [45]. The number of particles encountered per time is given by [22]

$$\dot{N} = \mathcal{L}\sigma \tag{4.1}$$

with the cross section σ for the present event and the instantaneous luminosity $\mathcal{L}$. The luminosity depends only on the characteristics of the collider and is often used as key parameter in collider physics [40].

$$\mathcal{L} = \frac{N_b n_b f_{\text{rev}} \gamma_r}{4\pi \epsilon_n \beta^*} F \tag{4.2}$$

Where N_b is the number of particles per bunch, n_b the number of bunches per beam, f_{rev} the rotational frequency, γ_r the Lorentz factor, ϵ_n the normalized transverse beam emittance, β^* the betatron function at the collision point and F respects the geometric luminosity reduction factor due to the crossing angle at the collision point. The luminosity measured at the ATLAS interaction point exceeded the design luminosity of $\mathcal{L} = 2.05 \times 10^{34} \, \text{cm}^{-2} \, \text{s}^{-1}$ by a factor of 2.05 on the 2$^{\text{nd}}$ of November 2017, proving the great success of the LHC machine setup over the years [46].

To meet the requirements of a general-purpose detector, several considerations for the detector design were taken into account: On the one hand there is the demand to be sensitive to the great variety of particles governed by the fundamental forces (see chapter 3.1). On the other hand the yet unknown physics should be potentially covered as well by the ATLAS detector – all seen from the angle of performing precision measurements. The basic structure of ATLAS is shown in figure 4.2 with its different sub-detector systems together with the convention for the coordinate system. The nominal interaction point acts as origin of the coordinate system, where the z-axis follows the beam line counterclockwise. Perpendicular to the z-axis lies the transverse x-y-plane usually described through the azimuthal angle ϕ. The positive x-axis points towards the center of the LHC. The cylindric symmetry of the detector suggests a cylindric coordinate system with the angle θ starting from the beamline. [45] Since the polar angle is not a Lorentz invariant quantity, it is useful
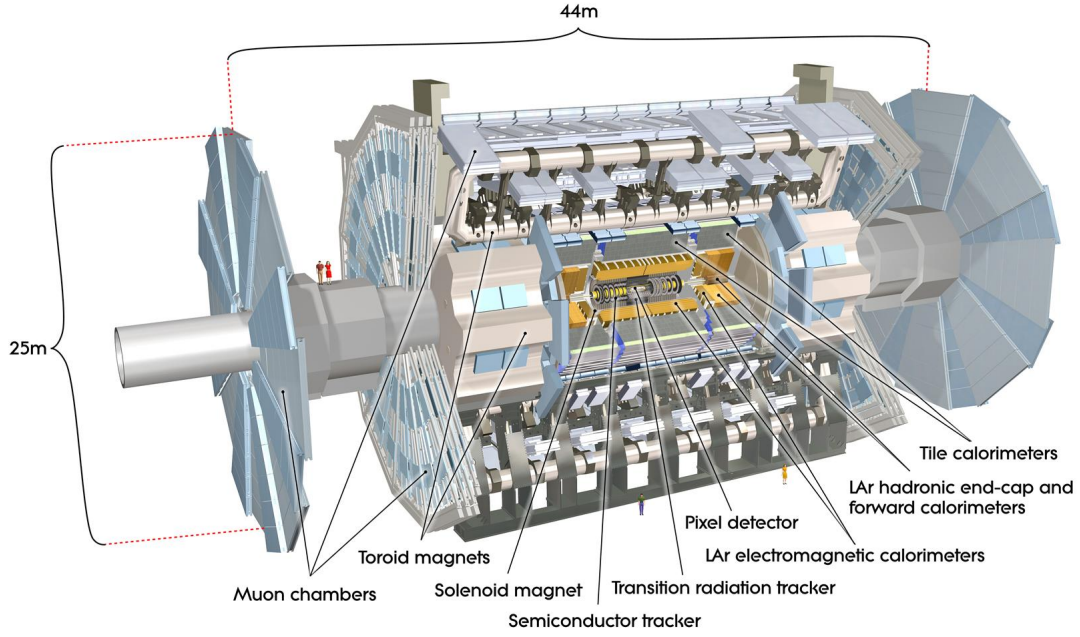
(a) The layered structure of the ATLAS detector at the LHC with its sub-systems inner detector, calorimeter, magnets and muon spectrometer [45].
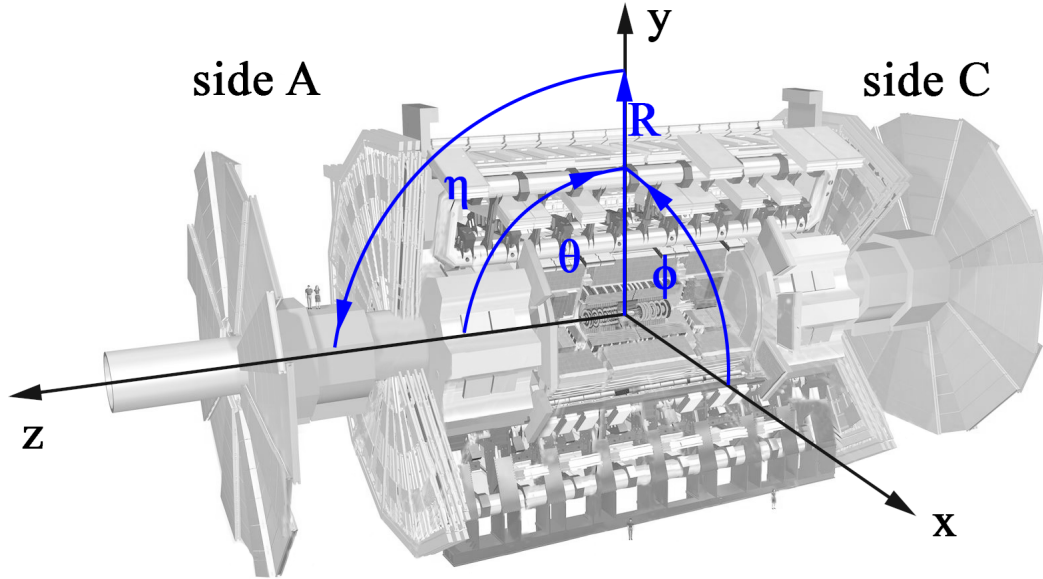
(b) The global ATLAS coordinate system formulated in cylindric coordinates with the z-axis parallel to the beam line and the transverse plane defined through azimuthal angle ϕ and pseudorapidity η. Based on [45].

Figure 4.2.: Structure of the ATLAS detector and the coordinate system.

to describe the position in terms of rapidity [40] $w = \frac{1}{2} \ln \frac{E+p_z c}{E-p_z c}$ in that highly relativistic regime. In the limit of large momenta, i.e. $|\mathbf{p}|c \approx E$, the rapidity coincides with the pseudorapidity formulated as [47]

$$\eta = -\ln \tan \frac{\theta}{2}. \tag{4.3}$$

This variable only depends on the polar angle is therefore the adequate quantity in the context of collision experiments, where usually the angle θ from the beamline is measured. [47]

The collision products, originating from the interaction point at the center of the ATLAS detector, will propagate through the different layers of the detector's subsystems. The inner detector is responsible to track electrically charged particles. The magnetic fields for identifying the particles' electric charge and for momentum measurement is provided by the ATLAS magnet system. The next layer includes the calorimeter. The electromagnetic calorimeter measures mainly the energy deposit of electrons, positrons and photons and allows the distinction between them with the help of the track information given by the inner detector. Hadronic particles will deposit their energy in the hadronic calorimeter. The outermost layer consists of the muon system responsible for a second independent measurement of the muon and anti-muon tracks. [45]

The magnet system includes a superconducting solenoid with a field strength of 2 T sourrounding the inner detector as well as three large superconducting toroid magnets composed in an eight-fold azimuthal symmetry around the calorimeter. The barrel toroid magnet delivers a field strength of 0.5 T and in the end-cap a field of 1 T is present. [45]
The inner detector is responsible for momentum measurements, vertex measurements and pattern recognition for the identification of electrically charged particles. This is achieved with a combination of semiconductor pixel and microstrip trackers (SCT). The Insertable B-Layer (IBL) is the innermost layer of the pixel detectors at a radius of 3.3 cm away from the beam line. Additional straw tube tracking detectors are sensitive to transition radiation (TRT) located in the outer part that are responsible for high vertex and momentum resolution. The $R - \phi$ segmented pixel detectors are of a size of $50 \times 400\,\mu\mathrm{m}^2$ and the SCTs with their 8 strip layers cover together a range of $|\eta| < 2.5$. Typically 36 hits per track are provided by the 4 mm straw tubes of the TRTs, which cover the range $|\eta| \leq 2.0$. [48][45]
Liquid argon electromagnetic sampling **calorimeters** with high granularity allow

for an excellent energy measurement of electrons and photons. They have a total thickness of more than 22 radiation lengths X_0 in the barrel region ($|\eta| < 1.475$) and more than $24X_0$ in the end-cap region ($1.375 < |\eta| < 3.2$). For hadronic energy measurements a scintillator-tile calorimeter covering $|\eta| < 1.7$ is in operation. It is a sampling calorimeter and uses steel as absorber material and scintillating tiles as active material in conjunction with wavelength shifting fibres. Further LAr technology is used for hadronic particles in the outer pseudorapidity range up to $|\eta| = 3.2$. Here copper plates provide the absorber material. The forward calorimeters extend the coverage of hadronic and electromagnetic energy measurements to $|\eta| = 4.9$ and are $10X_0$ deep. [45]

The **muon system** is located in the outer layer of the ATLAS detector and provides resolution for high energy muon tracks with three layered precision chambers up to the range of $|\eta| < 2.7$. This is possible because of the air-cored toroid magnet system including one barrel and two end-cap magnets generating strong bending power in a large volume and delivering a mostly perpendicular magnetic field with respect to the muon trajectories. The bending power $\int \vec{B} d\vec{l}$ along the track of the muon $d\vec{l}$ reaches from $1.5\,\mathrm{T\,m}$ to $5.5\,\mathrm{T\,m}$ in the range $|\eta| < 1.4$ (barrel) and up to $7.5\,\mathrm{T\,m}$ (end-cap). The precision chambers are Monitored Drift Tubes (MDT) and in the larger pseudorapidity range Chathode Strip Chambers (CSC), which are multiwire proportional chambers. Due to the fact that the overall performance crucially depends on the alignment of the muon detectors with respect to each other and with respect to the Inner Detector, MDTs are equipped with a optical monitoring system with 12000 sensors. Resistive Plate Chambers (RPC) and Thin Gap Chambers (TGC) are the constituents of the muon trigger system. [45]

Due to technology and resource limitations the data recording rate has to be reduced from $40\,\mathrm{MHz}$ to $1\,\mathrm{kHz}$. This poses high demands on an efficient **trigger system** which is organized in two levels. This is the level 1 hardware-based trigger and the software-based high level trigger (HLT). Level 1 uses only a subset of the total detector information making basic decisions to flag so called regions of interest within the detector's coordinate system. Searches include patterns for high transverse momenta of muon tracks, electrons and photons as well as jets or large missing energy balances. The output rate after this first selection accounts for $100\,\mathrm{kHz}$. The HLT is responsible for selecting the level 1 triggered regions at full granularity and precision, reconstructing the complete events. This event filter is the final stage and achieves data reduction down to the final data-taking rate of $1\,\mathrm{kHz}$, writing events of the size of approximately $2.4\,\mathrm{GB\,s^{-1}}$ to the disks. The HLT selection criteria are implemented using offline analysis procedures. [45][49]

5.

Turning detector signatures into physical objects

All components of the detector system of ATLAS (see chapter 4.2) deliver electronic signals of the proton-proton collisions, which have to be reconstructed to physical objects for the analysis. This chapter describes the reconstruction of the physical objects like electrons, muons, jets and b-flavor jets and taus, which are important for the analysis in this thesis. Furthermore, the role of Monte Carlo simulations in the analysis are presented briefly.

5.1. Electron reconstruction at ATLAS– identifying electrons

Electrons and positrons are common collision products due to their long lifetime. Therefore, relying on signatures of such particles in the detector is reasonable. Electrons and positrons* give rise to tracks in the Inner Detector of ATLAS and deposit energy in the electromagnetic calorimeter. The tracks and calorimeter signals are used in combination for the electron reconstruction. [50]

For the reconstruction of electrons in the central region ($|\eta| < 2.47$) several steps are needed. At first, respecting the granularity of the calorimeter, it is searched for electron cluster seeds in do called step of *seed-cluster reconstruction*. The efficiency of this search is $95\,\%$ to $99\,\%$ for transverse energies of $7\,\mathrm{GeV}$ and $> 15\,\mathrm{GeV}$ respectively. The *track reconstruction* is responsible for the pattern recogniztion respecting

---

*In this section, the term 'positron' is absorbed in the term 'electron'.

the energy loss due to mainly bremsstrahlung in the detector material up to 30 %. The track seed, consisting of three hits in different layers of the silicon detectors, is extended to the full track of at least seven hits to the region of interest at the electromagnetic calorimeter. This is done by the ATLAS Global χ^2 Track Fitter [51]. Afterwards the matching of the track to a specific cluster in the electromagnetic calorimeter is done in the *electron specific track fit*. The final step, *electron candidate reconstruction*, is the matching of the track candidate to the initial cluster seed. [50]

Both, the information of the track and the energy cluster, are used for the four-momentum calculation of the electrons. Algorithms for reconstructed electron identification are applied to distinguish signal-like or background-like electron candidates. For that the TRT likelihood method plays an important role, which uses the high-threshold hits of each TRT. Several discriminating variables are evaluated[†] for this likelihood method (LH). Based on the outcome, three operating points for the electron identification are defined: *Loose* relies on information of the hadronic calorimeter and the first two layers of the electromagetic calorimeter. *Medium* adds information from the TRTs, the transverse impact parameter and the third layer of the electromagnetic calorimeter, whereas the *Tight* operting point additionally considers track-cluster matching variables. [50]

For a well reconstructed electron also requirements on the isolation of the cluster and the track are necessary. In this thesis the definition of the operating point *Gradient* is relevant. The efficiency linarly depends on the transverse energy E_T. For Gradient the isolation in the calorimeter and the track is $0.1143\,\% \cdot E_T + 92.14\,\%$. [50]

5.2. Muon reconstruction at ATLAS – identifying muons

Muons are good tracers of particles with shorter lifetimes and thus should be reconstructed as an important information carrier of the particle collisions. Muons[*] are reconstructed independently in the inner detector and the muon spectrometer and the resulting combination of the two gives the full muon track. [52]

[†]For further details see [50]

[*]In this section, the term 'anti-muon' is absorbed in the term 'muon'.

The first step is again pattern recognition for seeds in the silicon layers from the inside towards the outside of the inner detector. Seeds are formed of three space points. The space points are provided from the pixel detectors with their local two-dimensional space points and from the combination of a pair of SCTs. The default setting of the seeding algorithm allows three combinations for space points: all space points in the pixel detector, all in the SCTs or two in the pixel detector and one in the SCT. [53]

The muon reconstruction in the muon spectrometer is initiated by the search of hit patterns in the muon chambers to form segments. Muon track candidates are created by fitting together from the segments in different layers, which is done by an combinatorial search. Selecting criteria include hit multiplicity and fit quality to find the optimal track. The hits associated with each track candidate, after applying an overlap removal algorithm, is fitted using a global χ^2 fit. [52]

The combination of the muon reconstruction depends on what information of the muon candidate is available in the inner detector and the muon spectrometer. A *combined muon* is reconstructed of the independent inner detector and muon spectrometer measurement in a global refit. *Segment-tagged muons* are extrapolated from the inner detector muon track to at least one local segment of the muon spectrometer. If the track of the inner detector can be matched to energy deposit in the calorimeter, the reconstructed muon is called *calorimeter-tagged* muon. Muons reconstructed only on the basis of the muon spectrometer are extrapolated back to the interaction point and therefore are called *extrapolated muons.*[52]

Quality requirements on the muon supress background contributions and garantee a robust momentum measurement and include discriminating variables like the χ^2 of the combined track. This categorization finalizes the muon identification process. For the category *Loose muons* all above listed muon types are used. The category *medium muons* minimizes the systematic uncertainties and is based only on combined muons and extrapolated muons. *Tight muons* only uses the combined muon type and is optimized for maximum purity at the cost of some efficiency. The *high-p_T muons* are designed for a maximazation of the momentum resolution for tracks above 100 GeV. [52]

The relevant isolation requirement for this thesis on muons is the so called *Gradient* isolation, which inlcudes track-based and calorimeter-based discriminating variables. In this case it is the sum of transverse momenta of the tracks in a cone around the muon with $\Delta R = \sqrt{\Delta\eta^2 + \Delta\phi^2} < 0.3$, excluding the muon track itself. The calorimeter condition is based on the sum of transverse energies of the topological clusters around the muon in a cone of $\Delta R < 0.2$. [52][54]

5.3. Jet reconstruction at ATLAS – identifying jets

Note that jets are not physical objects in the sense of elementary particles, but denote collimated streams of colored final states. Due to confinement (cf. chapter 3.1) colored fragments will always result in jet signatures. [3]
For the reconstructin of hadronic part of final states like isolated hadrons, jets (see also section 5.4) and hadronically decaying taus (see also section 5.5), the ATLAS experiment employs clusters of topological connected calorimeter cell signals (topo-clusters). The topo-cluster algorithm analyzes the spatial distribution of the cell signals to reconstruct the energy and direction of the incoming particle. [55]

The segmented lateral readout of the highly granularity calorimeter allows the distinction between signals from particle showers and background events by the reference of the cell signal significance $\zeta_{\text{cell}}^{\text{EM}}$. [55] Seeds are defined by cells, where the absolut energy $|E|$ exceeds the noise level by a factor of four standard deviations. The topo-clusters are expanded by iteratively all neighbour cells with energies two standard deviations above the noise level. [56]
For this thesis the relevant clustering algorithm is the anti-k_t algorithm. The algorithm needs the following definitions [57]:

$$d_{ij} = min(k_{ti}^{-2}, k_{tj}^{-2})\frac{\Delta_{ij}^2}{R^2} \tag{5.1}$$

$$d_{iB} = k_{ti}^{-2}\,, \tag{5.2}$$

where d_{ij} is the distance between the particles i and j and d_{iB} the distance between i and the beam B. k_t denotes the transverse momentum, R is the radius parameter and $\Delta_{ij}^2 = (\eta_i - \eta_j)^2 + (\phi_i - \phi_j)^2$ denotes the cone between i and j. The final clustered jet is achieved with the search of the minimum in distances d_{iB} and d_{ij}. If the mimimum is d_{ij}, then the sum of the four-momentum of object i and j is calculated and is treated as a new object. Again all distinces between the objects are re-calculated until d_{iB} is a minimum. This is means, object i is the final jet. The anti-k_t algorithm is a stable jet reconstruction algorithm and is not prone to fluctuations due to adding low k_t-objects. [57]

5.4. b-tagging at ALTAS – identifying b-jets

The third generation quarks, i.e. top (t) and bottom (b), play a crucial role in the SM and its various extension possibilities like the Leptoquark Model due to their large masses [58]. Therefore, it is essential to identify hadrons containing b quarks and seperating them from light-flavor quarks at hadron collider detectors like ATLAS. This task is commonly reffered as b-tagging and can be seen as a classification problem with the goal to assign right jet flavors. To that end the particle tracks in the Inner Detector and the jet reconstruction of clusters in the electromagnetic and hadronic calorimeter are discriminating objects. [59]
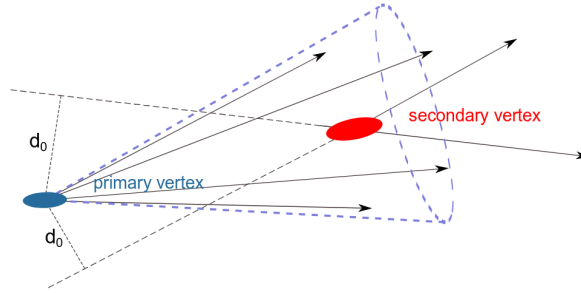
Figure 5.1.: Signature of a b-jet with the primary and secondary vertex created relevant for b-tagging. d_0 is the impact parameter. [58]

The long lifetime of B hadrons in the order of $1.6\,\mathrm{ps}$ allow them to travel a few millimeters in the detector. The subsequent decay of those heavy particles within a secondary vertex produce tracks with comparably large impact parameter d_0 that is the shortest distance of the particle track from the primary vertex (see figure 5.1). This signature and the deduced impact parameter significance $S(d_0) = \frac{d_o}{\sigma(d_0)}$, where $\sigma(d_0)$ is the uncertainty of the impact parameter, are used by the b-tagging algorithms including five low-level and two high-level taggers. [58] The b-tagging algorithms rely on multivariate combinations of the information and process them to calculate a discriminant value for each jet. Thresholds on these values are then defining the working point to provide efficiencient identification of b-jets. For better information processing of the combinations of large input parameters neural network classes can be used. [60] One example for a b-tagging algorithm is the the MV2 tagger which uses 24 input variables of the low-level taggers together with kinematic
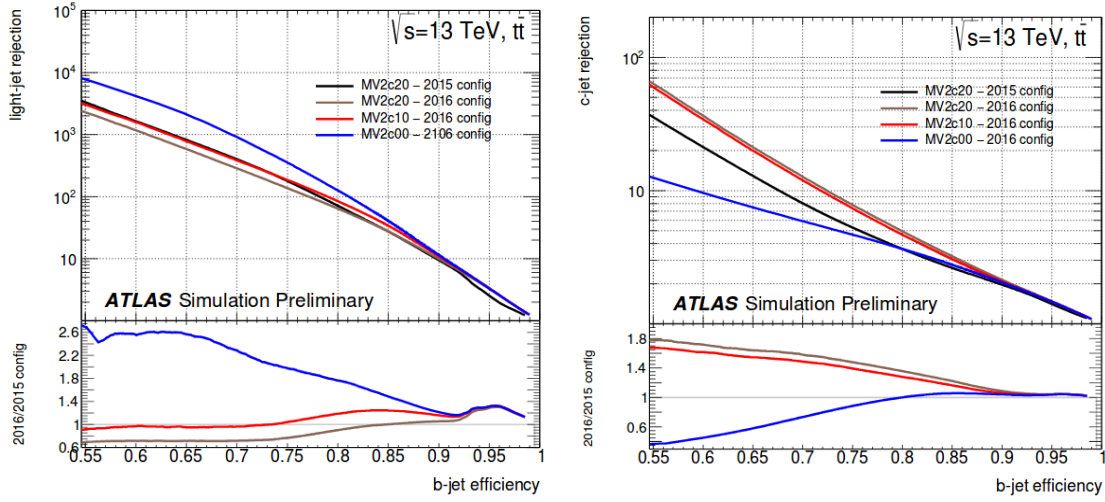
(a) Light-jet rejection versus b-jet efficiency for the MV2c10 tagger (red) in comparison to previous configurations evaluated on $t\bar{t}$ events. The ratio is evaluated in respect to MV2c10. [62]

(b) c-jet rejection versus b-jet efficiency for the MV2c10 tagger (red) in comparison to previous configurations evaluated on $t\bar{t}$ events. The ratio is evaluated in respect to MV2c10. [62]

Figure 5.2.: Light-flavor and c-jet rejection versus b-jet efficiency for the MV2c10 tagger. [62]

properties[*]. [59] It uses a boosted decision tree (BDT) to discriminate b-jets from light-jets and c-jets. [61] The light-flavor and c-jet rejection as a function of b-jet efficiency for MV2c10 (red line) is shown in figure 5.2. The description 'c10' indicates the fraction of c-jet composition of the training background sample, e.g. for MV2c10 the c-jet to light-jet composition ist $10\,\%/90\,\%$. Three other tagger configurations are shown as comparision as well as their ratio to MV2c10. Follwing the MV2c10 efficiency curve different working points can be defined. The relevant working point for the physical object selection in this work is $77\,\%$ (cf. chapter 6.2). The c-jet rejection rate for this working point is 6, for light-jet rejection 134 and for τ-rejection 22 extracted from $t\bar{t}$ events. [62]

---

[*]For further details on MV2 see [61]

5.5. Tau reconstruction at ATLAS – identifying taus

Final states with tau leptons*, decaying hadronically, play an important role for the physics at the ATLAS experiment. Five hadronic decay modes cover over $90\,\%$ of the overall hadronic modes, which results in one (1-prong) or three (3-prong) charged hadrons ($h^\pm$) up to two neutral pions (π^0) and a tau neutrino ν_τ. [63] For the reconstruction of hadronic taus $\tau_{\mathrm{had\text{-}vis}}$ at the ATLAS detector, the anti-k_t algorithm (see eq. (5.2)) for jet formation is used (see section 5.3) with a distance parameter of $R = 0.4$. The requirements for the transverse momentum is $p_T > 10\,\mathrm{GeV}$ and for the pseudorapidity is $|\eta| < 2.5$. The hadronic identification of the tau relies on topo-clusters in the last layer of electromagnetic calorimeter and the hadronic calorimeter. The additional track selection requires at least two associated hits in the pixel detector/IBL in the $\tau_{\mathrm{had\text{-}vis}}$ direction and at least seven hits in total in the pixel detector and the SCTs. Also requirements on the distance of closest approach are set to $|d_0| < 1.0\,\mathrm{mm}$ in the transverse plane and to $|\Delta z_0 \sin\theta| < 1.5\,\mathrm{mm}$.[64]

Due to the fact that the reconstruction of tau candidates provides very little rejection against jet background a detailed set of discriminating variables† are introduced. Tau identification relies on seperate boosted decision trees (BDT) for each prong case. The working points for that are labelled *loose*, *medium* and *tight* corresponding to different signal efficiency values. In case of 1-prong they are, respectively, 0.6, 0.55 and 0.45 for loose, medium and tight. The working points for 3-prong decays are 0.5, 0.4, 0.3 correspondigly. [64]

To ensure that electrons will be not misinterpreted as 1-prong tau decays an additional BDT is implemented as a tau-electron veto. It has the same classification of *loose*, *medium* and *tight*, but with signal efficiencies of 0.95, 0.85 and 0.75 respectively. [65]

5.6. Monte Carlo simulations

Final states of high energy particle collision experiments, like the LHC, is an extremely challenging endeavor. Typically hundreds of particles of different species are involved and their energy and momentum spectra a widely distributed over

---

*In this section, the 'term anti-tau' is absorbed in the term 'tau'.

†They can be found in [64].

differnt orders of magnitudes. Understanding these complex processes are crucial to make physical predictions and search for new physics. Therefore Monte Carlo (MC) simulations are one important cornerstone to handle these scenarios. [66]

MC simulations are based on an algorithm relying on sequences of pseudo random numbers. Effectively it is a method to numerical compute multidimensional integrals over a complicated region as it is often the case for matrix elements in perturbation theory. [67] The MC chain for the ATLAS detector has three main steps. This includes the generation of MC events with event generators, the simulation of the detector and the propagation of the particles with the associated interactions and the digitization of energy deposited in the detector's sensitive areas. The last step involves the simulation of the resulting signals in the readout system for comparison with real data. The detailed implemented simulation of the detector with GEANT4[68] additionally considers realistic detector conditions and misalignments as well as the detector response to be as realistic as possible. This fact enhances the digital copy to furthermore test the effectiveness of proposed search strategies for specific signatures. [69]

6.

Analysis

The framework conditions for the analysis, investigating the research question formulated in section 3.3.6, have to be defined. The MC samples and data samples, which are taken into account, are listed in detail in section 6.1. The physical object definition and the event selection for the performed analysis are presented in section 6.2 and 6.3.

6.1. Used data and Monte Carlo samples

Athena is the ATLAS software framework for event generation, simulation, reconstruction and derivation production (cf. also section 5.6) [70]. The management and build of the software packages rely on CMake. At the end of the software chain analyses use the AthAnalysisBase, which is organized in different anlysis sub-groups like the top-quark group. Their standard package for physical object reconstruction is AnalysisTop, which also includes the data analysis tool ROOT.

For this work a package based on AnalysisTop of release 21.2.56 (build on November 29, 2018) was used.
The analysis uses two types of MC samples. One category includes the LQ singal following the decays after the mBRW model (cf. section 3.3.2). These signal samples were produced with the event generator MADGRAPH5_aMCNLO [71]. The top pair is allowed to deacy either full leptonically in the dilepton LQ sample or semi-leptonically in the nonallhad LQ sample (cf. section 3.3.6). The other categories includes main background contributions of SM processes. That is background from $t\bar{t}$ pairs and inclusive $t\bar{t}H$ decay processes. The $t\bar{t}$ samples are generated with POWHEG-BOX and underlying event ...

6.2. Physical object selection

The physical object selection for electrons, muons, hadronic taus, jets and b-jets in the analysis is described in this chapter. For the basic reconstruction of physical objects see chapter 5.

Electrons

Electrons have to fullfill the tight quality requirement and have at least a transverse momentum of $p_T > 25\,\text{GeV}$ and lie in the pseudorapidity range of $|\eta| < 2.5$. In order to get a clean signal from a leptonic decaying top quark, the electrons have to meet the gradient isolation requirement. All single electron triggers are used for this selection.

Muons

Muons have to meet the medium quality requirement and have a transverse momentum of $p_T > 25\,\text{GeV}$. The selected muons are rconstructed within a pseudorapidity region of $|\eta| < 2.5$. Analogous to the electron selection for a clean lepton signal, the muon has to further fullfill the gradient isolation requirement and all single muon triggers are used for the selection.

Taus

Taus selected for this analysis have a transverse momentum of at least $p_T > 25\,\text{GeV}$ and must lie in the pseudorapidity range of $|\eta| < 2.5$. Additional to that the taus have to decay hadronically. Following their basic reconstruction procedure, taus have to met the conditions of the loose working point. To avoid misinterpretations of electrons as taus, the corresponding working point is set to loose.

6.3. Event selection

7.

Results

A.

Appendix

List of Figures

List of Tables

Bibliography

[1] Robert Mann. *An Introduction to Particle Physics and the Standard Model -*. CRC Press, Boca Raton, Fla, 2011.

[2] V. Parameswaran Nair. *Concepts in Particle Physics - A Concise Introduction to the Standard Model*. World Scientific Publishing Company, Singapore, 2017.

[3] Ian Brock and Thomas Schörner-Sadenius. *Physics at the Terascale*. Wiley, New York, 2011.

[4] W. N. Cottingham and D. A. Greenwood. *An Introduction to the Standard Model of Particle Physics -*. Cambridge University Press, Cambridge, 2007.

[5] David Griffiths. *Introduction to Elementary Particles -*. Wiley, New York, 2. aufl. edition, 2008.

[6] M. Tanabashi et al. Review of particle physics. *Phys. Rev. D*, 98:030001, Aug 2018.

[7] Maksym Teklishyn. Measurement of the η c (1s) production cross-section via the decay η c to proton-antiproton final state. 09 2014.

[8] Y. Fukuda et al. Evidence for oscillation of atmospheric neutrinos. *Phys. Rev. Lett.*, 81:1562–1567, Aug 1998.

[9] Q. R. Ahmad et al. Direct evidence for neutrino flavor transformation from neutral-current interactions in the sudbury neutrino observatory. *Phys. Rev. Lett.*, 89:011301, Jun 2002.

[10] G. L. Fogli, E. Lisi, A. Marrone, D. Montanino, A. Palazzo, and A. M. Rotunno. Global analysis of neutrino masses, mixings and phases: entering the era of leptonic CP violation searches. *Phys. Rev.*, D86:013012, 2012.

[11] Claus Kiefer. *Quantum Gravity -*. OUP Oxford, New York, London, 3$^{\text{rd}}$ edition, 2007.

[12] Andrew Fowlie, Csaba Balazs, Graham White, Luca Marzola, and Martti Raidal. Naturalness of the relaxion mechanism. *JHEP*, 08:100, 2016.

[13] Prasad Hegde, Karl Jansen, C. J. David Lin, and Attila Nagy. Stabilizing the electroweak vacuum by higher dimensional operators in a Higgs-Yukawa model. *PoS*, LATTICE2013:058, 2014.

[14] Steven Weinberg. Implications of dynamical symmetry breaking. *Phys. Rev. D*, 13:974–996, Feb 1976.

[15] J D Vergados. *The Standard Model and Beyond -*. World Scientific Publishing Company, Singapore, 2017.

[16] Yorikiyo Nagashima. *Beyond the Standard Model of Elementary Particle Physics -*. John Wiley & Sons, New York, new. edition, 2014.

[17] Masahiro Kuze and Yves Sirois. Search for particles and forces beyond the standard model at HERA ep and Tevatron $p\bar{p}$ colliders. *Prog. Part. Nucl. Phys.*, 50:1–62, 2003. [Erratum: Prog. Part. Nucl. Phys.53,583(2004)].

[18] Hisaki Hatanaka, Takeo Inami, and C. S. Lim. The Gauge hierarchy problem and higher dimensional gauge theories. *Mod. Phys. Lett.*, A13:2601–2612, 1998.

[19] W. de Boer. Grand unified theories and supersymmetry in particle physics and cosmology. *Prog. Part. Nucl. Phys.*, 33:201–302, 1994.

[20] R. N. Mohapatra. Neutrino mass and grand unification. *Phys. Scripta*, T121:185–191, 2005.

[21] Howard Georgi and S. L. Glashow. Unity of all elementary-particle forces. *Phys. Rev. Lett.*, 32:438–441, Feb 1974.

[22] Donald H. Perkins. *Introduction to High Energy Physics* -. Cambridge University Press, Cambridge, 4th edition, 2000.

[23] Goran Senjanovic. Proton decay and grand unification. *AIP Conf. Proc.*, 1200:131–141, 2010.

[24] K. Kobayashi et al. Search for nucleon decay via modes favored by supersymmetric grand unification models in Super-Kamiokande-I. *Phys. Rev.*, D72:052007, 2005.

[25] John C. Baez and John Huerta. The Algebra of Grand Unified Theories. *Bull. Am. Math. Soc.*, 47:483–552, 2010.

[26] Jogesh C. Pati and Abdus Salam. Lepton number as the fourth "color". *Phys. Rev. D*, 10:275–289, Jul 1974.

[27] JoAnne L. Hewett and Thomas G. Rizzo. Low-energy phenomenology of superstring-inspired e6 models. *Physics Reports*, 183(5):193 – 381, 1989.

[28] Hesselbach, S., Franke, F., and Fraas, H. Neutralinos in E6 inspired supersymmetric U(1)' models. *Eur. Phys. J. C*, 23(1):149–162, 2002.

[29] W. Buchmüller and R. Rückl and D. Wyler. Leptoquarks in lepton-quark collisions. *Physics Letters B*, 191(4):442 – 448, 1987.

[30] Michael E. Peskin and Daniel V. Schroeder. *An Introduction to Quantum Field Theory* -. Addison-Wesley Publishing Company, Reading, 1995.

[31] Bastian Diaz, Martin Schmaltz, and Yi-Ming Zhong. The leptoquark Hunter's guide: Pair production. *JHEP*, 10:097, 2017.

[32] J. L. Hewett and S. Pakvasa. Scalar-leptoquark production at hadron colliders. *Phys. Rev. D*, 37:3165–3171, Jun 1988.

[33] M. Kramer, T. Plehn, M. Spira, and P. M. Zerwas. Pair production of scalar leptoquarks at the CERN LHC. *Phys. Rev.*, D71:057503, 2005.

[34] Morad Aaboud et al. Search for scalar leptoquarks in pp collisions at $\sqrt{s} = 13$ TeV with the ATLAS experiment. *New J. Phys.*, 18(9):093016, 2016.

[35] ATLAS Collaboration, G. Aad, B. Abbott, et al. Searches for scalar leptoquarks in pp collisions at $\sqrt{s} = 8$ TeV with the atlas detector. *The European Physical Journal C*, 76(1):5, Jan 2016.

[36] Albert M Sirunyan et al. Search for third-generation scalar leptoquarks decaying to a top quark and a τ lepton at $\sqrt{s} = 13$ TeV. 2018.

[37] Ann Heinson. Useful diagrams of top signals and backgrounds. `http://www-d0.fnal.gov/Run2Physics/top/top_public_web_pages/top_feynman_diagrams.html`. Last update: October 29, 2011.

[38] CERN. About CERN. `https://home.cern/about`. retrieved on September 4, 2018.

[39] CERN. CERN Complex. `http://www.lhc-facts.ch/img/news2015/lhccomplex_.jpg`. Last update: October 29, 2011.

[40] Lyndon Evans and Philip Bryant. LHC Machine. *Journal of Instrumentation*, 3(08):S08001, 2008.

[41] The ALICE Collaboration, K Aamodt, et al. The ALICE experiment at the CERN LHC. *Journal of Instrumentation*, 3(08):S08002, 2008.

[42] Gerfried J Wiener, Julia Woithe, Alexander Brown, and Konrad Jende. Introducing the lhc in the classroom: an overview of education resources available. *Physics Education*, 51(3):035001, 2016.

[43] The LHCb Collaboration, A Augusto Alves Jr, et al. The LHCb Detector at the LHC. *Journal of Instrumentation*, 3(08):S08005, 2008.

[44] The CMS Collaboration, S Chatrchyan, et al. The CMS experiment at the CERN LHC. *Journal of Instrumentation*, 3(08):S08004, 2008.

[45] The ATLAS Collaboration, G Aad, et al. The ATLAS Experiment at the CERN Large Hadron Collider. *Journal of Instrumentation*, 3(08):S08003, 2008.

[46] Rende Steerenberg. LHC report: LHC reaches 2017 targets. `https://home.cern/cern-people/updates/2017/11/lhc-report-lhc-reaches-2017-targets`. posted by Stefania Pandolfi on 7 Nov 2017. Last updated 26 Jun 2018.

[47] Cheuk-Yin Wong. *Introduction to High-Energy Heavy-Ion Collisions*. WORLD SCIENTIFIC, 1994.

[48] Alessandro La Rosa. The ATLAS Insertable B-Layer: from construction to operation. *JINST*, 11(12):C12036, 2016.

[49] Georges Aad et al. Technical Design Report for the Phase-I Upgrade of the ATLAS TDAQ System. Technical Report CERN-LHCC-2013-018. ATLAS-TDR-023, Sep 2013. Final version presented to December 2013 LHCC.

[50] Electron efficiency measurements with the ATLAS detector using the 2015 LHC proton-proton collision data. Technical Report ATLAS-CONF-2016-024, CERN, Geneva, Jun 2016.

[51] T G Cornelissen, M Elsing, I Gavrilenko, J-F Laporte, W Liebig, M Limper, K Nikolopoulos, A Poppleton, and A Salzburger. The global χ^2 track fitter in atlas. *Journal of Physics: Conference Series*, 119(3):032013, 2008.

[52] Georges Aad et al. Muon reconstruction performance of the ATLAS detector in proton-proton collision data at $\sqrt{s} =$13 TeV. *Eur. Phys. J.*, C76(5):292, 2016.

[53] Performance of the ATLAS Silicon Pattern Recognition Algorithm in Data and Simulation at $\sqrt{s} = 7$ TeV. Technical Report ATLAS-CONF-2010-072, CERN, Geneva, Jul 2010.

[54] Hannah Elizabeth Herde. Muon reconstruction performance in ATLAS at Run-II. *PoS*, EPS-HEP2015:285, 2015.

[55] Georges Aad et al. Topological cell clustering in the ATLAS calorimeters and its performance in LHC Run 1. *Eur. Phys. J.*, C77:490, 2017.

[56] M. Aaboud and others. Jet reconstruction and performance using particle flow with the atlas detector. *The European Physical Journal C*, 77(7):466, Jul 2017.

[57] Matteo Cacciari, Gavin P. Salam, and Gregory Soyez. The anti- k t jet clustering algorithm. *Journal of High Energy Physics*, 2008(04):063, 2008.

[58] Per Ola Hansson Adrian. The ATLAS b-Jet Trigger. In *Proceedings, 31st International Conference on Physics in collisions (PIC 2011): Vancouver, Canada*, 2011.

[59] Michela Paganini. Machine Learning Algorithms for *b*-Jet Tagging at the ATLAS Experiment. In *18th International Workshop on Advanced Computing and Analysis Techniques in Physics Research (ACAT 2017) Seattle, WA, USA*, 2017.

[60] Luca Scodellaro. b tagging in ATLAS and CMS. In *5th Large Hadron Collider Physics Conference (LHCP 2017) Shanghai, China, May 15-20, 2017*, 2017.

[61] Expected performance of the ATLAS *b*-tagging algorithms in Run-2. Technical Report ATL-PHYS-PUB-2015-022, CERN, Geneva, Jul 2015.

[62] Optimisation of the ATLAS *b*-tagging performance for the 2016 LHC Run. Technical Report ATL-PHYS-PUB-2016-012, CERN, Geneva, Jun 2016.

[63] Georges Aad et al. Reconstruction of hadronic decay products of tau leptons with the ATLAS experiment. *Eur. Phys. J.*, C76(5):295, 2016.

[64] Reconstruction, Energy Calibration, and Identification of Hadronically Decaying Tau Leptons in the ATLAS Experiment for Run-2 of the LHC. Technical Report ATL-PHYS-PUB-2015-045, CERN, Geneva, Nov 2015.

[65] Zinonas Zinonos. Reconstruction and identification of hadronic decays of tau leptons in ATLAS. In *Proceedings, 2nd Conference on Large Hadron Collider Physics Conference (LHCP 2014): New York, USA, June 2-7, 2014*, 2014.

[66] Andy Buckley et al. General-purpose event generators for LHC physics. *Phys. Rept.*, 504:145–233, 2011.

[67] Glen Cowan. *Statistical Data Analysis - .* Oxford University Press, New York, 1998.

[68] J. Allison et al. Recent developments in Geant4. *Nuclear Instruments and Methods in Physics Research Section A: Accelerators, Spectrometers, Detectors and Associated Equipment*, 835:186 – 225, 2016.

[69] Z. Marshall. The atlas simulation software. *Nuclear Physics B - Proceedings Supplements*, 197(1):254 – 258, 2009. 11th Topical Seminar on Innovative Particle and Radiation Detectors (IPRD08).

[70] ATLAS Software Project. ATLAS Software documentation. `https://atlassoftwaredocs.web.cern.ch/athena/`. Last update: April 24, 2017.

[71] J. Alwall, R. Frederix, S. Frixione, V. Hirschi, F. Maltoni, O. Mattelaer, H. S. Shao, T. Stelzer, P. Torrielli, and M. Zaro. The automated computation of tree-level and next-to-leading order differential cross sections, and their matching to parton shower simulations. *JHEP*, 07:079, 2014.